This article has been accepted for publication in a future issue of this journal, but has not been fully edited. Content may change prior to final publication. Citation information: DOI 10.1109/TMI.2020.2967322, IEEE Transactions on Medical Imaging

Intraoperative Correction of Liver Deformation Using Sparse Surface and Vascular Features via Linearized Iterative Boundary Reconstruction

Jon S. Heiselman,* William R. Jarnagin, and Michael I. Miga

***Abstract*—During image guided liver surgery, soft tissue deformation can cause considerable error when attempting to achieve accurate localization of the surgical anatomy through image-to-physical registration. In this paper, a linearized iterative boundary reconstruction technique is proposed to account for these deformations. The approach leverages a superposed formulation of boundary conditions to rapidly and accurately estimate the deformation applied to a preoperative model of the organ given sparse intraoperative data of surface and subsurface features. With this method, tracked intraoperative ultrasound (iUS) is investigated as a potential data source for augmenting registration accuracy beyond the capacity of conventional organ surface registration. In an expansive simulated dataset, features including vessel contours, vessel centerlines, and the posterior liver surface are extracted from iUS planes. Registration accuracy is compared across increasing data density to establish how iUS can be best employed to improve target registration error (TRE). From a baseline average TRE of 11.4 ± 2.2 mm using sparse surface data only, incorporating additional sparse features from three iUS planes improved average TRE to 6.4 ± 1.0 mm. Furthermore, increasing the sparse coverage to 16 tracked iUS planes improved average TRE to 3.9 ± 0.7 mm, exceeding the accuracy of registration based on complete surface data available with more cumbersome intraoperative CT without contrast. Additionally, the approach was applied to three clinical cases where on average error improved 67% over rigid registration and 56% over deformable surface registration when incorporating additional features from one independent tracked iUS plane.**

***Index Terms*—Deformation, image guided surgery, liver, registration, ultrasound**

I. Introduction

In nearly every treatment option for hepatic cancer, therapeutic risk and efficacy balance on the ability to accurately localize the intraoperative positions of anatomical structures and interventional targets. Surgical resection of the liver, which remains the best curative option for hepatic malignancies aside from transplantation, must be carefully planned with respect to the positions of tumors and vessels hidden beneath the surface of the organ. This planning stage is essential for ensuring adequate margins, maximizing volume and blood perfusion in the liver remnant, and minimizing risk of hemorrhage and biliary injury. However, in open and laparoscopic liver surgery alike, intraoperative deformation of the liver is unavoidable due to procedural aspects such as hemostatic perihepatic packing in open approaches, abdominal insufflation in laparoscopic approaches, retraction, and mobilization from stabilizing ligaments. These deformations can compromise intraoperative translation of surgical plans that are based on the preoperatively imaged anatomy. Significant deformations of the liver have been shown to exist between preoperative and intraoperative presentations during both open and laparoscopic surgery. In a previous study, the average magnitude of these preoperative-to-intraoperative deformations across the anterior surface of the liver were found to exceed 10 mm during laparoscopy and 7 mm during open surgery, with maximum values greater than 20 mm [1].

Various methods have been developed to compensate for intraoperative deformation of the liver in the context of image guidance, where information derived from the preoperative anatomy is updated to match the intraoperative conformation of the organ through registration techniques. Beyond rigid registration, biomechanical models based on linear elasticity have proven to be well suited for deformable registration due to a favorable compromise between registration accuracy, computational time complexity, and intraoperative time constraints. While elastic registration methods based on organ surface data collected in the operating room are becoming more common [1–8], the type and algorithmic treatment of intraoperative data sources in the registration process is becoming equally important with regard to alignment fidelity [9]. In particular, the accuracy of surface-based methods has been found to depend crucially on the amount of intraoperative data made available for registration; previous work has suggested that registration accuracy can improve if wider coverage of the liver surface can be measured [1–3]. However, limited field of view in the surgical environment can directly conflict with the goal of acquiring broad surface coverage. Whereas intraoperative volumetric imaging such as

Manuscript received October 14, 2019; revised January 10, 2020; accepted January 12, 2020. This work was supported by the National Institutes of Health grants NCI-R01CA162477, NIBIB-T32EB021937, and NIBIB-R01EB027498. *Asterisk indicates corresponding author*.

*J. S. Heiselman is with the Department of Biomedical Engineering at Vanderbilt University, Nashville, TN 37235 USA (e-mail: jon.s.heiselman@vanderbilt.edu).

W. R. Jarnagin is with the Department of Surgery at Memorial Sloan Kettering Cancer Center, New York, NY 10065 USA.

M. I. Miga is with the Department of Biomedical Engineering at Vanderbilt University, Nashville, TN 37235 USA.

cone beam CT has been proposed to offer more complete intraoperative data for the registration task [10,11], these approaches are costly, require specialized facilities, present a major disruption to existing surgical workflow, and are unlikely to reach the capability of updating in real time at the speed of intraoperative organ interactions.

Tracked intraoperative ultrasound offers the real-time ability to identify features at depth inside the liver and represents a powerful contribution in the image guidance toolkit. Already, intraoperative ultrasound (iUS) is commonly used during liver resection to stage disease, identify lesions invisible on CT, and determine relationships to the vascular and biliary anatomy [12]. However, due to a confluence of factors that can make lesions sonographically occult, iUS is not yet suitable as a comprehensive guidance solution and needs to be complemented by information from preoperative imaging assessments [13]. Although interpreting and localizing freehand iUS can be challenging, tracked iUS adds quantitative spatial understanding to the physical positions of features that are visible in the ultrasonic modality even if the lesion is unapparent. These features can reliably include contours of the portal and hepatic veins and the posterior surface of the liver if imaged at sufficient depth. This capability makes it possible to use subsurface features from tracked iUS as additional constraints to improve registration accuracy beyond the capacity offered by surface data alone.

Several groups have developed methods to register iUS data with preoperative CT or MR images. Early spline methods matched 3D iUS volumes with image intensities based on similarity metrics such as normalized cross correlation [14,15], linear combination of linear correlation [16], edge-intensity joint entropy [17], and local structure orientation descriptors [18]. However, many of these registration techniques were designed for percutaneous procedures where small deformations and good initial alignments were possible. To accommodate larger deformations, Lange et al. parameterized vessel features between CT and 3D iUS volumes as centerline representations to assist optimization of a thin plate spline deformation model based on a normalized gradient field image similarity measure [19]. However, registration by inter-modality similarity metrics can be slow and may not exactly match differential tissue responses to distinct imaging physics. Additionally, spline models of deformation may not produce registrations as accurate as their biomechanical counterparts [20]. More recent iUS registration methods have elected to forego image intensity information and instead relate preoperatively segmented geometric features such as vessel contours and centerlines to tracked iUS in sparse configurations where rapid intraoperative segmentation of ultrasound features becomes possible. Among these, only rigid registration techniques using vessel centerlines [21], a combination of centerlines and surface data [22], and centerline bifurcation landmarks [23] have been developed. While iUS features have been used for intraoperative validation of surface registration methods [24], deformable liver registration based on biomechanical models have yet to incorporate iUS as an intraoperative data source.

Accurate alignment of the organ surface does not guarantee a successful registration. The internal displacement field between the modeled anatomy and the true deformed state must also be accurate throughout the volume. Mechanics-based models, unlike interpolative spline methods, ensure that these fields develop realistically according to constitutive laws of physics and their applied boundary conditions. However, mechanics-based methods are not without potential shortcomings. For example, some approaches treat intra-operative data sources as boundary forces [2–5] or boundary displacements [25,26] directly on the organ. When employed this way, these configurations of boundary conditions impart organ deformation at the sites of data collection as opposed to the regions where actual mechanical loads are applied. With the underlying sources of deformation largely ignored, these methods may not develop accurate displacement fields beyond the immediate region of data collection. These limitations have given rise to methods that commit particular attention to anatomical constraints [6], data-constrained energy minimization [11], and inverse modeling approaches that reconstruct the unknown distributed loads applied to the organ [1,8]. In practice, due to the many forms of physical and temporal intraoperative constraints, it is also imperative that these registration methods are simultaneously fast and robust.

In this paper, a generalized algorithm is presented for reconstructing and correcting intraoperative deformation of the liver for improving registration accuracy during hepatic image guidance. While this approach adopts an inverse biomechanical model similar to [1] and [8], a new deformation framework is presented based on the Saint-Venant principle, which states that a local region of mechanical loading can be replaced with a statically equivalent load wherein the difference between loading responses exponentially vanishes with distance towards the far field. Using this principle to decompose elastic perturbations facilitates improved fidelity and robustness, and permits more controlled and realistic deformations of the liver. Other advances include subsurface error constraints that allow registration of internal hepatic features, closed form gradient computations over numerical approximations, and formalized linearization of the boundary reconstruction problem to yield a method that rapidly approximates intraoperative deformations with high accuracy given sparse intraoperative data. Equally important to presenting this novel approach, this paper demonstrates how clinical tracked iUS data can be applied to achieve a high performance registration algorithm. In accordance with these contributions, a rigorous experimental framework has been produced that involves a combination of physical and simulation data in a controlled environment of 6291 simulated registration scenarios. These data represent multiple liver geometries, multiple deformations, and varying amounts of sparse surface and subsurface feature data from iUS. To study the approach, registration accuracy is characterized across a wide range of sparse subsurface data configurations. Finally, a proof-of-concept experiment is illustrated with three clinical cases to demonstrate viability.

This article has been accepted for publication in a future issue of this journal, but has not been fully edited. Content may change prior to final publication. Citation information: DOI 10.1109/TMI.2020.2967322, IEEE Transactions on Medical Imaging

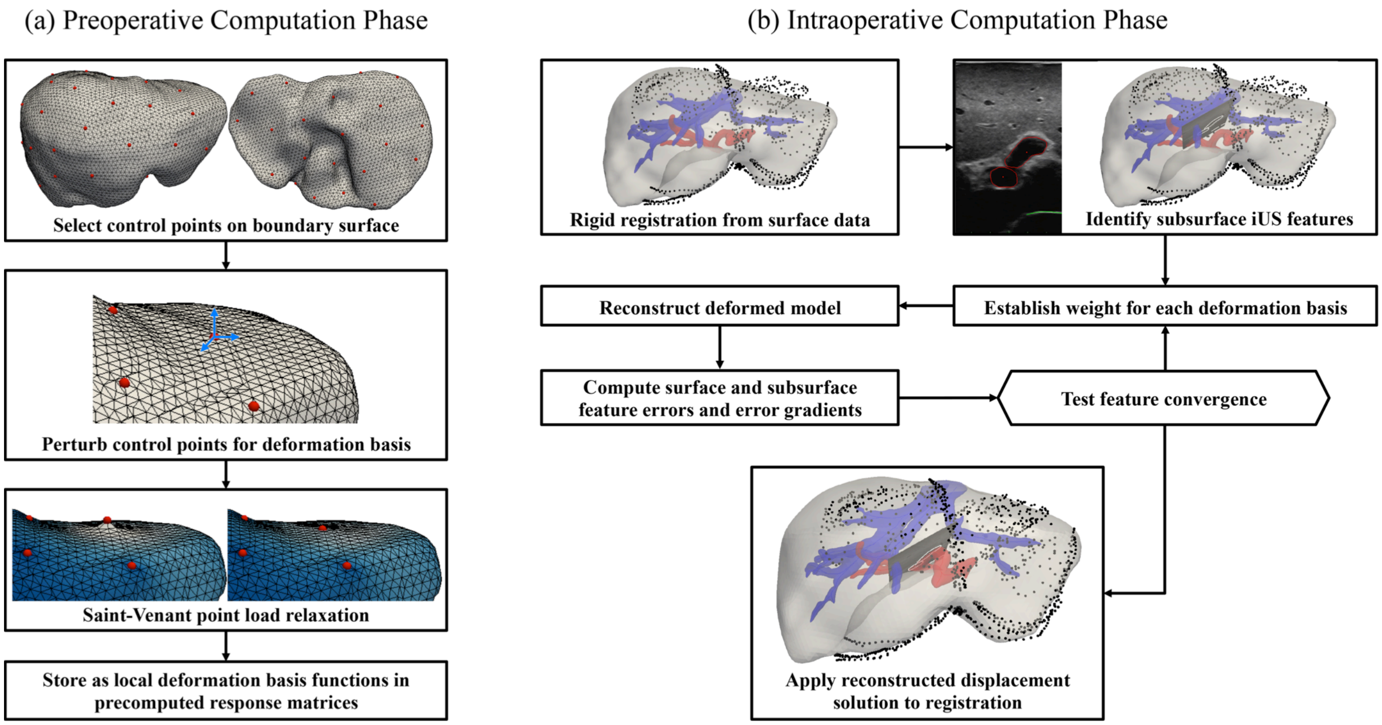

Fig. 1. Overview of the proposed algorithm for boundary condition reconstruction in a deformable registration framework for hepatic image guidance. (a) In the preoperative computation phase, a series of control points are evenly distributed across the surface of the organ. Linear elastic responses to control point perturbations in three orthogonal directions establish a basis of deformations across the mesh. Point loads are then relaxed to their Saint-Venant far field equilibria. These steps are computed in advance of the procedure. (b) Sparse data of the organ surface are collected intraoperatively and a rigid registration between image and physical patient spaces is performed. Features in tracked iUS planes are manually designated and transformed into sparse point clouds. Based on these surface and subsurface points, weights for a linear combination of the precomputed basis deformations are optimized to minimize error between intraoperative data and the deformable model.

II. Proposed Algorithm

A. Overview of the Registration Task

Given a preoperative model of the hepatic anatomy, the registration task is to determine a displacement field that produces an optimal alignment of the preoperative model to the deformed conformation of the intraoperative physical liver. This preoperative model is comprised of triangulated meshes for the hepatic parenchyma, portal vein, and hepatic vein generated from custom surgical planning software [27]. Centerline representations of the preoperative portal and hepatic veins are created with the open source Vascular Modeling Toolkit [28], and a tetrahedral finite element mesh of the liver parenchyma is produced with a custom mesh generation software [29]. Tetrahedral meshes are discretized to 4 mm edge length and consist of approximately 25 000 vertices for a typical liver.

In a liver navigation system [30], sparse intraoperative data of the organ surface is collected using an optically tracked stylus and sparse subsurface data from tracked iUS imaging. The tracked iUS setup consists of an Aloka T-probe transducer (Hitachi Aloka Medical Ltd., Wallingford, Connecticut) attached to an optically tracked rigid body calibrated using the N-wire phantom method [31]. Experiences with this tracked iUS system have already been reported in [24] and [32]. New to this work, intraoperative positions of the portal and hepatic vein contours and the posterior surface of the liver are segmented from iUS image planes when visible, using lines drawn on a graphical display and rasterized into points via the Bresenham line algorithm [33]. Vessel centerline points are approximated as in-plane centroids of the segmented vessel contours. To minimize intraoperative workflow burden, it is important to note that only a handful of iUS planes are used. With rigid registration as the current FDA-approved standard for image guidance during liver procedures, a salient feature weighted iterative closest point rigid alignment [34] is established between the intraoperative organ surface data and the preoperative model for initialization.

From this initial rigid alignment, the proposed algorithm aims to reconstruct an initially unknown set of boundary conditions representing the intraoperative deformations experienced by the organ by using sparse surface and subsurface measurements. The overall registration approach is depicted in Fig. 1 and is described in more detail in the following sections.

B. The Boundary Reconstruction Problem

An isotropic linearly elastic finite element model is employed to simulate deformation of the liver. At static equilibrium, linear elasticity is governed by the Navier-Cauchy equations in three dimensions:

$$\frac{E}{2(1+\nu)}\nabla^2\boldsymbol{u}+\frac{E}{2(1+\nu)(1-2\nu)}\nabla(\nabla\cdot\boldsymbol{u})+\boldsymbol{F}=0 \tag{1}$$

where E is the Young modulus, ν is the Poisson ratio, $\boldsymbol{u}$ is displacement, and $\boldsymbol{F}$ is applied force. Following [8], the values E = 2100 kPa and ν = 0.45 are used. With the Galerkin

This article has been accepted for publication in a future issue of this journal, but has not been fully edited. Content may change prior to final publication. Citation information: DOI 10.1109/TMI.2020.2967322, IEEE Transactions on Medical Imaging

weighted residual method on linear Lagrange basis functions, this system of partial differential equations can be rewritten as:

$$K\boldsymbol{u} = \boldsymbol{f} \tag{2}$$

where K is the global stiffness matrix and $\boldsymbol{f}$ is a vector of known forcing conditions. In the forward boundary value problem, the displacement vectors $\boldsymbol{u}$ throughout the domain can be solved only if displacements and forces on the boundary are known. The inverse boundary reconstruction problem attempts to resolve the distributed loading conditions on the boundary that establish the displacement response $\widetilde{\boldsymbol{u}}$ that best approximates the partially observable true displacement field $\boldsymbol{u}$ without exact spatial correspondence being known.

C. Linearized Basis of Displacements

By the principle of superposition, a basis of displacements could be constructed such that $\widetilde{\boldsymbol{u}} = J_u^* \boldsymbol{\alpha}^*$, where the matrix J_u^* represents displacement responses to independent unit displacements of every boundary node in each spatial direction and the vector $\boldsymbol{\alpha}^*$ represents the weight for each basis with length triple the number of boundary nodes. Solving for $\boldsymbol{\alpha}^*$ would represent the full resolution boundary reconstruction problem where every boundary node on the mesh is permitted independent degrees of freedom. However, reconstructing the full resolution problem is not feasible due to computational time constraints and limited information rendering the solution extremely underdetermined.

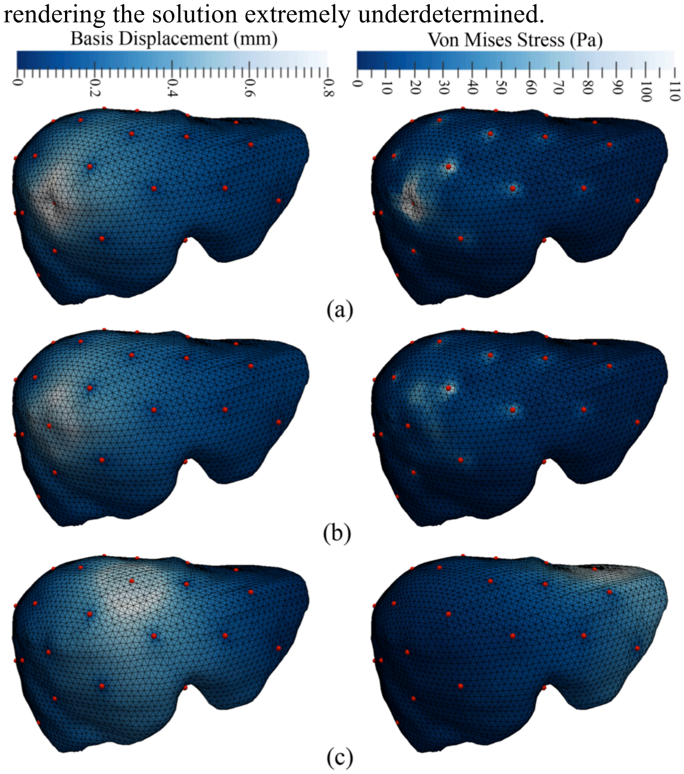

Fig. 2. Control point deformation modes. Control points shown in red are distributed across the surface of the mesh. (a) Displacement response (left) and stress response (right) to a control point perturbation of 5 mm in the +x direction. (b) Displacement response (left) and stress response (right) after Saint-Venant point load relaxation. (c) Relaxed displacement responses for other control point deformation modes on the mesh. Each mode represents a deformation basis in the local vicinity of the control point.

Dimensionality can be substantially reduced by pruning the reconstructive degrees of freedom to displacements on a subset of control points distributed across the boundary. In this way, the unknown distributed load applied to the domain is approximated as a statically equivalent linear combination of responses to locally consolidated point loads. By the Saint-Venant principle, differences between the deformation responses of the true and the approximated loading configurations quickly vanish with distance. To simulate the basis of localized boundary load responses, control points are evenly spaced on the surface of the mesh using k-means clustering, with $k = 45$. The control points are independently perturbed in each Cartesian direction to generate $3k$ total modes of deformation. Displacement responses for each mode are solved from (2) by applying a boundary condition with 5 mm displacement in the direction of the active control point perturbation and zero displacement boundary conditions at all remaining control points. With each resulting displacement solution, stress and strain are computed from conventional stress-strain and strain-displacement relations for linear elasticity. Fig. 2a shows the displacement and stress responses to one such point load perturbation. However, by focusing the total boundary condition effect from a local neighborhood into a single point, local artifact arises from approximating a smoothly varying distributed load on the surface as a series of point effects. To address these irregularities, point load responses are relaxed back onto to the boundary nodes in the local neighborhood of the control point.

To accomplish relaxation, the Saint-Venant principle is invoked again to determine a statically equivalent load that is redistributed across the locally aggregated boundary region surrounding the control point. Each point load is relaxed by establishing a radius of half the distance between control points, or equivalently the Voronoi tile of the k-means cluster, and solving (2) for the self-equilibrated response of the local region when the far field displacement responses of all other boundary nodes are immobilized. The displacement and stress solutions after relaxing the applied point load are shown in Fig. 2b and additional examples of relaxed displacement mode responses for other control point perturbations are shown in Fig. 2c. Each relaxed control point response becomes a mode of variation in the reconstructive basis, representing a spatially local deformation applied to the mesh. For the purpose of reconstruction from sparse data, this approach is beneficial in comparison to more spatially distributed spectral [35] and polynomial [8] function bases that can produce extrapolative error when fitting local data.

With these relaxed responses to control point boundary perturbations, a displacement response matrix J_u is constructed where each column of length $3M$ corresponds to a relaxed displacement solution vector to one of the $3k$ rows of control point perturbations, where M is the number of nodes in the mesh. The relaxed stress and strain solutions for each perturbation response are similarly assembled into the stress response matrix J_σ and the strain response matrix J_ε. With superposition, a reconstructed deformation state that also satisfies (1) can be linearized as:

$$\widetilde{\boldsymbol{u}} = J_u\boldsymbol{\alpha} \quad (3)$$

$$\widetilde{\boldsymbol{\sigma}} = J_\sigma\boldsymbol{\alpha} \quad (4)$$

$$\widetilde{\boldsymbol{\varepsilon}} = J_\varepsilon\boldsymbol{\alpha} \quad (5)$$

where $\widetilde{\boldsymbol{u}}$, $\widetilde{\boldsymbol{\sigma}}$, and $\widetilde{\boldsymbol{\varepsilon}}$ are the approximated displacement, stress, and strain values for the deformation defined by the relaxed control point response matrices J_u, J_σ, and J_ε, and $\boldsymbol{\alpha}$ is the deformation state vector of length $3k$.

D. Intraoperative Reconstruction

To solve for the deformation state, Levenberg-Marquardt optimization is employed to iteratively minimize model-data error and the strain energy of the system in a scheme that also optimizes rigid transformation parameters. This optimization of rigid parameters allows a global minimization of element rotations to reduce incurred rotational inaccuracies inherent to linear elasticity. While co-rotational models are sometimes used to compensate, these formulations incorporate geometric nonlinearities that disrupt the superposition leveraged in this application. Hence, the total deformation state to reconstruct is the parameter vector $\boldsymbol{\beta}$ of length $3k$+6 defined as

$$\boldsymbol{\beta} = [\boldsymbol{\alpha}, \boldsymbol{\tau}, \boldsymbol{\theta}] \quad (6)$$

where $\boldsymbol{\tau}$ is a vector of rigid translations and $\boldsymbol{\theta}$ is a vector of rigid rotations about the x, y, and z axes. These parameters are determined by minimizing the least squares objective function

$$\Omega(\boldsymbol{\beta}) = \sum_F \frac{w_F}{N_F}\sum_{i=1}^{N_F} f_i^{\,2} + w_E f_E^{\,2} \quad (7)$$

where f_i denotes the error between the deformed model and the data point i of N_F total points within an intraoperatively collected point cloud for feature F, w_F is the weight of the feature, f_E is the average strain energy of the deformation state, and w_E is a regularizing strain energy weight that controls the deformability of the registration. This objective function distinguishes the error terms for distinct types of features that can comprise the intraoperative data. From digitization of the organ surface, features include the falciform ligament, the left and right inferior ridges, and the general anterior liver surface. From tracked iUS, features can consist of the posterior liver surface, hepatic and portal vein contours, and hepatic and portal vein centerlines. Finally, single corresponding fiducial points can be used when they are available in controlled phantom environments that have embedded and measurable intraoperative target positions. To determine model-data error, a distance vector $\boldsymbol{p}_i$ is defined as

$$\boldsymbol{p}_i = \boldsymbol{y}_i - S_i(R(\boldsymbol{x}_0 - \overline{\boldsymbol{x}}_0 + J_u\boldsymbol{\alpha}) + \boldsymbol{\tau} + \overline{\boldsymbol{x}}_0) \quad (8)$$

where $\boldsymbol{y}_i$ is the intraoperative data point, $\boldsymbol{x}_0$ are the initial coordinates of the undeformed mesh, $\overline{\boldsymbol{x}}_0$ is the centroid of $\boldsymbol{x}_0$, S_i is a sampling operation encoding correspondence between model and data, and the rotation matrix R is defined as

$$R = R(\boldsymbol{\theta}) = R(\theta_x)R(\theta_y)R(\theta_z). \quad (9)$$

The sampling operation S_i is implemented as a closest point operator that selects the nearest feature point in the deformed model to $\boldsymbol{y}_i$. The sampling operation is updated every iteration and also applies the computed deformation to subsurface vessel models and preoperatively designated fiducial positions by interpolating displacements from the deformed mesh.

For feature data points corresponding to a geometric model surface, the model-data error term becomes a sliding constraint taken to be the magnitude of the vector projection onto $S_i\widehat{\boldsymbol{n}}$, the unit normal direction at the closest surface point:

$$f_{surface} = (S_i\widehat{\boldsymbol{n}})^T\boldsymbol{p}_i. \quad (10)$$

This sliding constraint is maintained for centerline feature data points by taking the magnitude of the vector rejection of $\boldsymbol{p}_i$ from $S_i\widehat{\boldsymbol{t}}$, the unit tangent vector at the closest point on the centerline model, which can be derived to be

$$f_{centerline} = \sqrt{\boldsymbol{p}_i^{\,T}\boldsymbol{p}_i - (\boldsymbol{p}_i^{\,T}S_i\widehat{\boldsymbol{t}})^2}. \quad (11)$$

Finally, the error term for single fiducial points is simply the Euclidean distance between the model-predicted and measured fiducial location

$$f_{fiducial} = \sqrt{\boldsymbol{p}_i^{\,T}\boldsymbol{p}_i}. \quad (12)$$

The energy penalty function is represented by the average strain energy density distributed over the mesh vertices,

TABLE I
CLOSED FORM EXPRESSIONS FOR MODEL-DATA ERRORS AND GRADIENTS

Function	f	$q_i^{\,T}$	$\partial f/\partial\boldsymbol{\alpha}$	$\partial f/\partial\boldsymbol{\tau}$	$\partial f/\partial\boldsymbol{\theta}$
$f_{surface}$	$(S_i\widehat{\boldsymbol{n}})^T\boldsymbol{p}_i$	$(S_i\widehat{\boldsymbol{n}})^T$	$-q_i^{\,T}S_iRJ_u$	$-q_i^{\,T}S_i$	$-q_i^{\,T}S_i\frac{\partial R}{\partial\boldsymbol{\theta}}(\boldsymbol{x}_0 - \overline{\boldsymbol{x}}_0 + J_u\boldsymbol{\alpha})$
$f_{centerline}$	$\sqrt{\boldsymbol{p}_i^{\,T}\boldsymbol{p}_i - (\boldsymbol{p}_i^{\,T}S_i\widehat{\boldsymbol{t}})^2}$	$\frac{\boldsymbol{p}_i^{\,T} - (\boldsymbol{p}_i^{\,T}S_i\widehat{\boldsymbol{t}})(S_i\widehat{\boldsymbol{t}})^T}{\sqrt{\boldsymbol{p}_i^{\,T}\boldsymbol{p}_i - (\boldsymbol{p}_i^{\,T}S_i\widehat{\boldsymbol{t}})^2}}$	$-q_i^{\,T}S_iRJ_u$	$-q_i^{\,T}S_i$	$-q_i^{\,T}S_i\frac{\partial R}{\partial\boldsymbol{\theta}}(\boldsymbol{x}_0 - \overline{\boldsymbol{x}}_0 + J_u\boldsymbol{\alpha})$
$f_{fiducial}$	$\sqrt{\boldsymbol{p}_i^{\,T}\boldsymbol{p}_i}$	$\frac{\boldsymbol{p}_i^{\,T}}{\sqrt{\boldsymbol{p}_i^{\,T}\boldsymbol{p}_i}}$	$-q_i^{\,T}S_iRJ_u$	$-q_i^{\,T}S_i$	$-q_i^{\,T}S_i\frac{\partial R}{\partial\boldsymbol{\theta}}(\boldsymbol{x}_0 - \overline{\boldsymbol{x}}_0 + J_u\boldsymbol{\alpha})$
f_E	$\frac{1}{2M}\boldsymbol{\alpha}^T(J_\varepsilon^{\,T}J_\sigma)\boldsymbol{\alpha}$	—	$\frac{1}{M}\boldsymbol{\alpha}^T(J_\varepsilon^{\,T}J_\sigma)$	0	0

This article has been accepted for publication in a future issue of this journal, but has not been fully edited. Content may change prior to final publication. Citation information: DOI 10.1109/TMI.2020.2967322, IEEE Transactions on Medical Imaging

$$f_E = \frac{1}{2M}\boldsymbol{\alpha}^T\left(J_\varepsilon{}^T J_\sigma\right)\boldsymbol{\alpha} \tag{13}$$

where M is the number of nodes in the mesh. For all registrations, the weights in (7) for the falciform and inferior ridges are chosen to be 0.3 m^{-2}, the strain energy weight 10^{-8} Pa^{-2}, and all other weights 1.0 m^{-2}.

From an initial estimate $\boldsymbol{\beta}_0 = \mathbf{0}$, Levenberg-Marquardt optimization iteratively solves for $\boldsymbol{\beta}$ by the step

$$\boldsymbol{\beta}_{k+1} - \boldsymbol{\beta}_k = \left(J^T W J + \lambda\,\mathrm{diag}(J^T W J)\right)^{-1} J^T W \boldsymbol{f} \tag{14}$$

where the minimized errors are $\boldsymbol{f} = [\boldsymbol{f}_i, f_E]$, the square diagonal matrix $W = \mathrm{diag}(\boldsymbol{w_F}/\boldsymbol{N_F}, w_E)$ are function weights, the regularization parameter λ is controlled by a trust region prediction ratio, and the Jacobian of the error is $J = \partial\boldsymbol{f}/\partial\boldsymbol{\beta}$. Table 1 shows closed form expressions for the error terms and their derivatives comprising J. The termination condition is established as $|\Omega(\boldsymbol{\beta}_{k+1}) - \Omega(\boldsymbol{\beta}_k)| < 10^{-12}$.

Regarding material properties, it is important to note that the displacement and strain solutions of the deformation model are independent from the Young modulus because only pure displacement boundary conditions and no boundary forces are applied in (1). However, the strain energy is directly proportional to modulus. Consequently, any difference in stiffness between the patient liver and the model can be compensated at the time of registration by adjusting the deformability parameter w_E.

III. Experimentation

The proposed algorithm is evaluated in a series of experiments on nine simulated deformations from three laparoscopic mobilizations transposed onto three unique liver geometries. In each of the nine deformations, 16 potential iUS plane orientations are sampled. In this dataset, registration accuracy is examined across a wide range of access to intraoperative data coverage. Furthermore, the algorithm is applied to clinical data from three cases of image-guided open liver resection, where accuracy of the method is estimated with real sources of intraoperative error.

A. Data Simulation

The data simulation process aims to map deformation fields from three different laparoscopic mobilizations of a liver phantom to three distinct liver geometries. With this approach, registration performance can be evaluated in a diverse yet controlled environment. Three human livers and their portal and hepatic veins were segmented from preoperative contrast-enhanced CT images of deidentified patients, and meshes and vessel centerlines were generated as described in section II-A. Collected with these patient data were sparse intraoperative surface patterns digitized with an optically tracked stylus spanning 25.2% (Liver 1), 14.9% (Liver 2), and 24.9% (Liver 3) of the total liver surface.

In a phantom environment, a silicone liver with 147 embedded targets was created from a 3D printed liver built from a preoperative scan of a different patient. This phantom was imaged without deformation, then placed in a mock insufflated abdomen with ligament attachments that reproduce laparoscopic changes to the liver. The phantom was re-imaged in three conditions of laparoscopic deformation: left mobilization (L), where the left triangular and falciform ligaments were dissected; no mobilization (N), where no ligaments were dissected; and right mobilization (R), where the right triangular and falciform ligaments were dissected. These phantom data were originally reported in [1]. In this paper, the phantom data provide detailed displacement fields for each laparoscopic mobilization scenario. These fields were obtained by registering the full surface and target positions from post-deformation images to their undeformed counterparts using the algorithm described in section II at a higher resolution of k = 90. This process yielded phantom registrations with highly accurate surface errors of 0.4 ± 0.6 mm (L), 0.4 ± 0.5 mm (N), 0.4 ± 0.7 mm (R) and target errors of 1.9 ± 1.0 mm (L), 2.1 ± 1.0 mm (N), and 2.1 ± 1.2 mm (R) based on data from CT scans with voxel resolution of 0.6 x 0.6 x 3 mm. However, these phantom displacement fields do not represent the exact deformations to be reconstructed in the simulation experiments. Instead, they represent a realistic deformation template to be distorted and applied to the previous liver geometries.

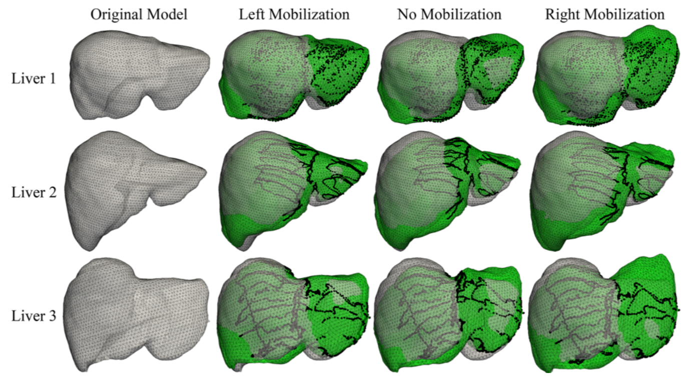

Fig. 3. Three liver geometries (white) and three applied displacement fields comprise nine simulated deformations (green). The applied deformations represent mobilization of stress-bearing ligaments on the left side, no sides, or right side of the liver in a laparoscopic phantom setup that reproduced the insufflated intra-abdominal anatomy surrounding the liver. Transposed clinical patterns of sparse surface data are shown in black.

Livers 1–3 were registered to the undeformed liver phantom using an affine registration followed by the optimization method from section II only to establish inexact correspondence between anatomical regions of the disparate liver shapes. Using these alignments, displacements from phantom deformations L, N, and R were mapped onto livers 1, 2, and 3 with their associated surface data patterns to produce the nine deformed livers shown in Fig. 3. It should be noted that the nine resultant livers are not purely linear elastic deformations of their original meshes. Nonlinear distortions in the displacement fields are created by the spatial mapping process between the physically deforming phantom and the novel liver geometries. In each of the nine simulated deformations, 16 iUS plane locations were sampled and geometric intersections

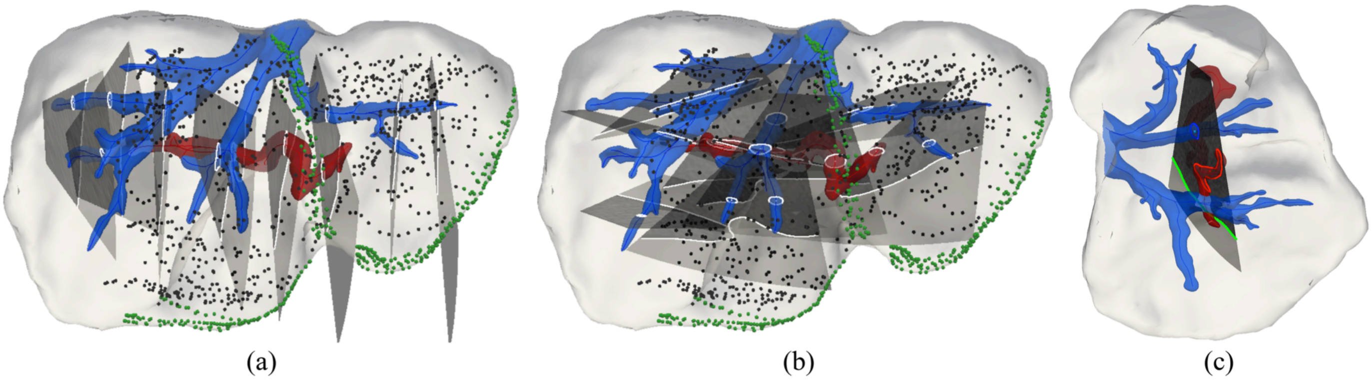

Fig. 4. Ultrasound plane locations sampled across the ground truth deformed Liver 1 with left mobilization (1–L). The hepatic vein is shown in blue, the portal vein in red, the anterior surface data in black, and the surface features in dark green. A total of 16 ultrasound plane locations are sampled for each simulated deformation, consisting of (a) 8 vertical planes and (b) 8 lateral planes. Subsurface features intersecting the iUS planes are shown in white. (c) A view of a single ultrasound plane orientation with hepatic vein contour (blue), portal vein contour (red), and posterior surface contour (green).

with the deformed portal and hepatic vein models and the posterior liver surface were determined using the Möller triangle intersection algorithm [36] then rasterized into points in the iUS plane using the Bresenham algorithm [33]. Positions of the sampled iUS features are displayed in Fig. 4.

A simulated dataset is created with the nine transposed phantom deformations to examine the registration method across varying levels of intraoperative data. These levels include registration scenarios using: 1) sparse anterior surface data only, 2) subsurface data from one iUS plane in addition to the sparse surface data, 3) subsurface data from two combined iUS planes in addition to the sparse surface data, 4) data from three combined iUS planes in addition to the sparse surface data, and 5) all 16 iUS planes in addition to the sparse surface data. Furthermore, a scenario based on the deformed full anterior and posterior surfaces is included without subsurface data to compare performance against information typically available from intraoperative CT without contrast, e.g. cone beam CT (CBCT). Finally, a scenario using all ground truth deformed information, including the full liver surfaces and vessel data, is considered to evaluate optimal performance if significantly more data from intraoperative contrast-enhanced CT (iCT) were available. In total, 6291 registration scenarios are included in the simulated dataset. For each, target registration error (TRE) is computed as the average distance of corresponding vertices between the registered and ground truth deformed meshes.

In the following sections, surface data registration is examined to identify how additional subsurface information could improve overall registration accuracy. Sparse iUS image planes are then incorporated and registration accuracy is characterized across varying levels of intraoperative access to surface and subsurface data. Finally, the iUS registration methods are applied to three cases of clinical data.

B. Limitations of Surface Registration

In Fig. 5, rigid and deformable registration results to a transposed surface data pattern are shown for one of the nine liver deformations. In this case, average TRE across the mesh was 12.4 ± 8.3 mm for rigid registration and 9.3 ± 7.3 mm for deformable registration. Qualitatively from Fig. 5c, it can be seen that registration accuracy has high spatial sensitivity, with accuracy dropping off considerably where surface data cannot be collected. This behavior has two implications. First, the spatial sampling of TRE is profoundly important, as the measured error of a single validation target can greatly vary depending on its position relative to the regions of the organ that are deforming, and how well the available data describes this deformation. Therefore, unbiased validation metrics that thoroughly sample target errors throughout the domain are needed to give a complete picture of registration accuracy. Second, the profile of data collection on the deformed organ must also be acknowledged. As shown in Fig. 5d, the proximity of a target to its nearest intraoperative data point is a strong predictor of its registration error (Pearson r = 0.83). This trend suggests that distant targets may not be well constrained by intraoperative data and that intraoperatively acquired data may not completely describe the unique deformation of the organ. Ideally, data coverage should be extensive enough to enable accurate localization of anatomical structures many centimeters beneath the surface. Although surface data coverage is often inherently constrained by anatomical obstructions and limited fields of view, tracked

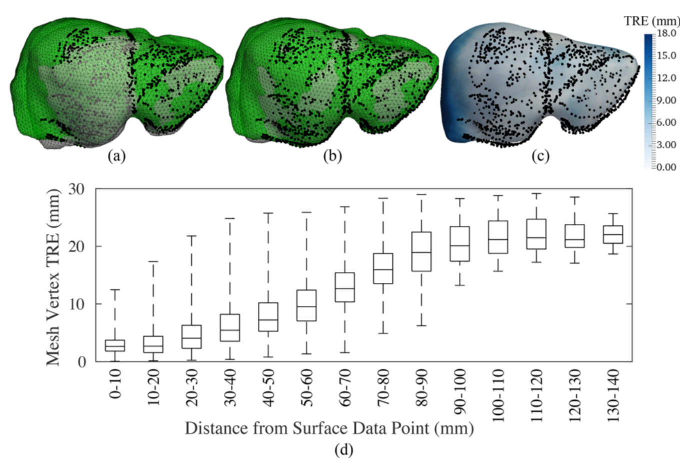

Fig. 5. An example case of registration to sparse surface data. The registered models (transparent white) are compared to the ground truth deformation (transparent green) for (a) rigid, and (b) deformable registrations to the applied clinical surface data pattern (black). In (c), the spatial distribution of TRE is shown for deformable registration to surface data. In (d), registration accuracy across the mesh is plotted against distance away from intraoperative data. Registrations are less accurate at greater distances away from data, suggesting that data coverage is a critical factor for whole organ TRE.

This article has been accepted for publication in a future issue of this journal, but has not been fully edited. Content may change prior to final publication. Citation information: DOI 10.1109/TMI.2020.2967322, IEEE Transactions on Medical Imaging

TABLE II
TARGET REGISTRATION ERRORS (MM) FOR SIMULATED LAPAROSCOPIC DEFORMATIONS

Deformation	Rigid	Surface (S)	S + 1 Plane (n = 16)	S + 2 Planes (n = 120)	S + 3 Planes (n = 560)	S + All Planes	CBCT	iCT
1–L	12.4 (±8.3)	9.3 (±7.3)	7.4 ± 1.6	6.4 ± 1.3	5.7 ± 1.0	3.5 (±2.3)	3.6 (±1.9)	2.4 (±1.7)
1–N	15.3 (±11.2)	13.5 (±10.8)	10.5 ± 2.4	8.8 ± 2.0	7.7 ± 1.6	4.7 (±3.0)	5.0 (±2.3)	3.4 (±2.0)
1–R	14.9 (±10.1)	10.8 (±8.9)	9.4 ± 2.2	8.0 ± 2.0	7.1 ± 1.6	4.2 (±2.9)	4.5 (±2.3)	3.0 (±2.0)
2–L	10.9 (±8.5)	10.4 (±8.2)	7.6 ± 1.9	6.0 ± 1.4	5.2 ± 1.0	3.1 (±2.0)	3.4 (±1.6)	2.1 (±1.4)
2–N	16.9 (±10.3)	15.8 (±11.3)	11.4 ± 2.6	9.3 ± 2.2	8.0 ± 1.6	5.2 (±3.5)	5.0 (±2.3)	3.1 (±2.0)
2–R	12.5 (±9.2)	12.3 (±8.9)	9.2 ± 2.5	7.6 ± 2.1	6.4 ± 1.6	3.7 (±2.6)	4.2 (±2.2)	2.3 (±1.8)
3–L	12.8 (±5.5)	8.5 (±6.4)	7.5 ± 1.3	6.1 ± 1.2	5.2 ± 0.9	3.1 (±2.0)	3.8 (±1.7)	2.4 (±1.5)
3–N	13.9 (±5.9)	12.0 (±6.6)	8.9 ± 1.0	7.2 ± 1.0	6.2 ± 0.8	4.4 (±2.4)	5.8 (±2.8)	3.7 (±2.2)
3–R	15.1 (±6.5)	10.3 (±7.8)	9.1 ± 2.0	7.2 ± 1.7	6.0 ± 1.4	3.6 (±2.3)	4.9 (±2.4)	3.1 (±2.0)
Average	**13.8 ± 1.9**	**11.4 ± 2.2**	**9.0 ± 1.4**	**7.4 ± 1.2**	**6.4 ± 1.0**	**3.9 ± 0.7**	**4.5 ± 0.8**	**2.8 ± 0.5**

Target registration errors (mean ± std) for registrations using increasing intraoperative data content. Standard deviations in parentheses represent variability across mesh vertex targets within a single case (n = 1); all other standard deviations represent variability in the average mesh TRE across the constituent cases.

iUS makes it possible to more effectively describe deformations in deeper regions of the liver to reduce the uncertainty of distant targets.

While TRE of surface registrations in the simulated dataset seem to be higher than those reported in [1], it should be noted that the distributions of targets are significantly different. The average distance of validation targets to the closest surface data point is 44.8 mm for the simulated data, while this metric was only 28.6 mm for the laparoscopic phantom data in [1]. Using Fig. 5d as a qualitative guide, the performance in [1] would be anticipated to be superior to the TRE reported here.

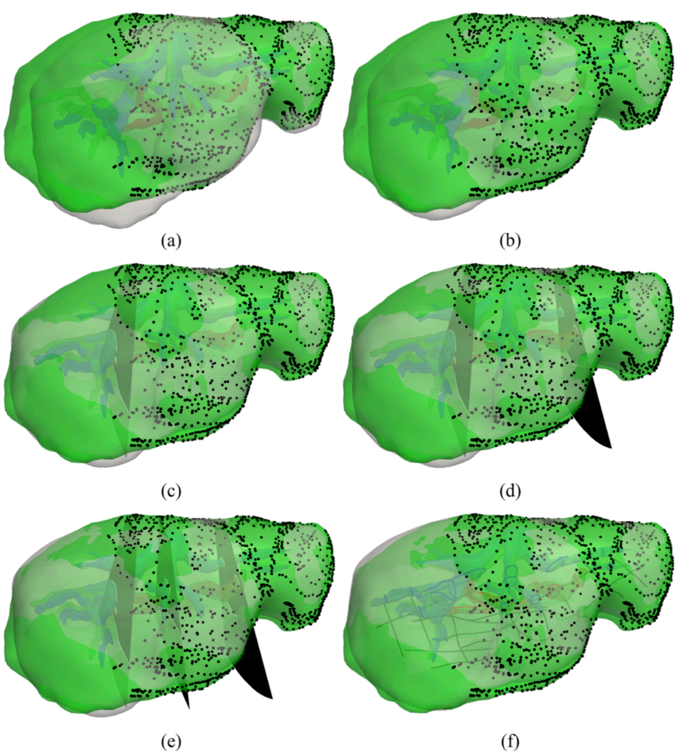

Fig. 6. Registrations to data from simulated left-mobilized deformation on Liver 1 (1–L). The ground truth deformed liver is shown in green and the registered model is shown in white. Registrations were performed to surface data with (a) rigid, (b) deformable, (c) deformable with one tracked iUS plane, (d) deformable with two tracked iUS planes, (e) deformable with three tracked iUS planes, and (f) deformable with all 16 tracked iUS planes. Average TRE across the mesh for these examples were (a) 12.4 ± 8.3 mm, (b) 9.3 ± 7.3 mm, (c) 5.9 ± 3.6 mm, (d) 5.7 ± 3.7 mm, (e) 5.2 ± 3.7 mm, and (f) 3.5 ± 2.3 mm.

C. Data Simulation Results

To illustrate the effect of incorporating constraints from iUS data on registration accuracy, TRE is reported over a comprehensive range of access to intraoperative data. Registrations were performed on the 6291 registration scenarios using contour, centerline, and posterior features from iUS planes in the optimization of (7). Fig. 6 shows registration results as increasing numbers of ultrasound planes are used in an example case. Results across all cases are summarized in Table II. In each row of Table II, a progressive decrease in TRE is observed as a greater amount of subsurface information is added to the deformable registration. These results are mirrored in Fig. 7, which shows probability distribution functions for target errors across the mesh vertices of all registrations in each category of intraoperative data. Clear leftward shifts and decreased weights in the tails of the distributions are seen as data content increases, and all pairwise distributions of target error significantly differ from

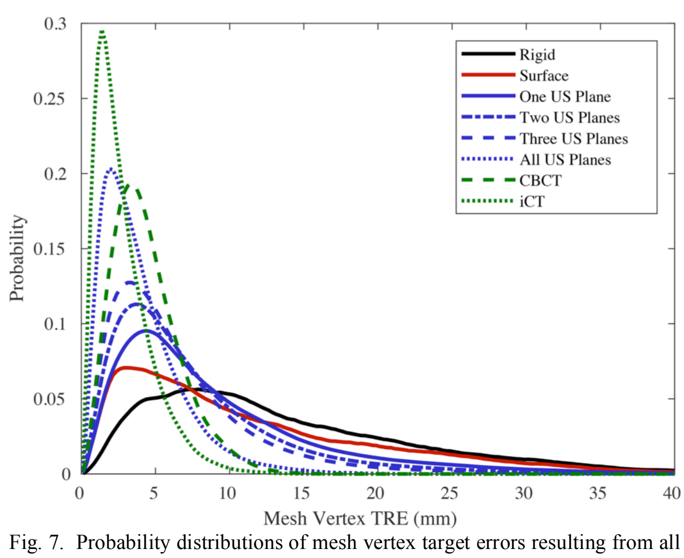

Fig. 7. Probability distributions of mesh vertex target errors resulting from all registrations to the nine simulated deformations with varying levels of intraoperative data. The clinical patterns of sparse anterior surface data are used for registrations in the black, red, and blue curves. The blue curves incorporate sparse features from increasing numbers of tracked iUS planes. The green CBCT curve uses the full anterior and posterior surfaces of the ground truth deformed mesh, and the green iCT curve uses the full surfaces in addition to the ground truth deformed vessel contours and vessel centerlines.

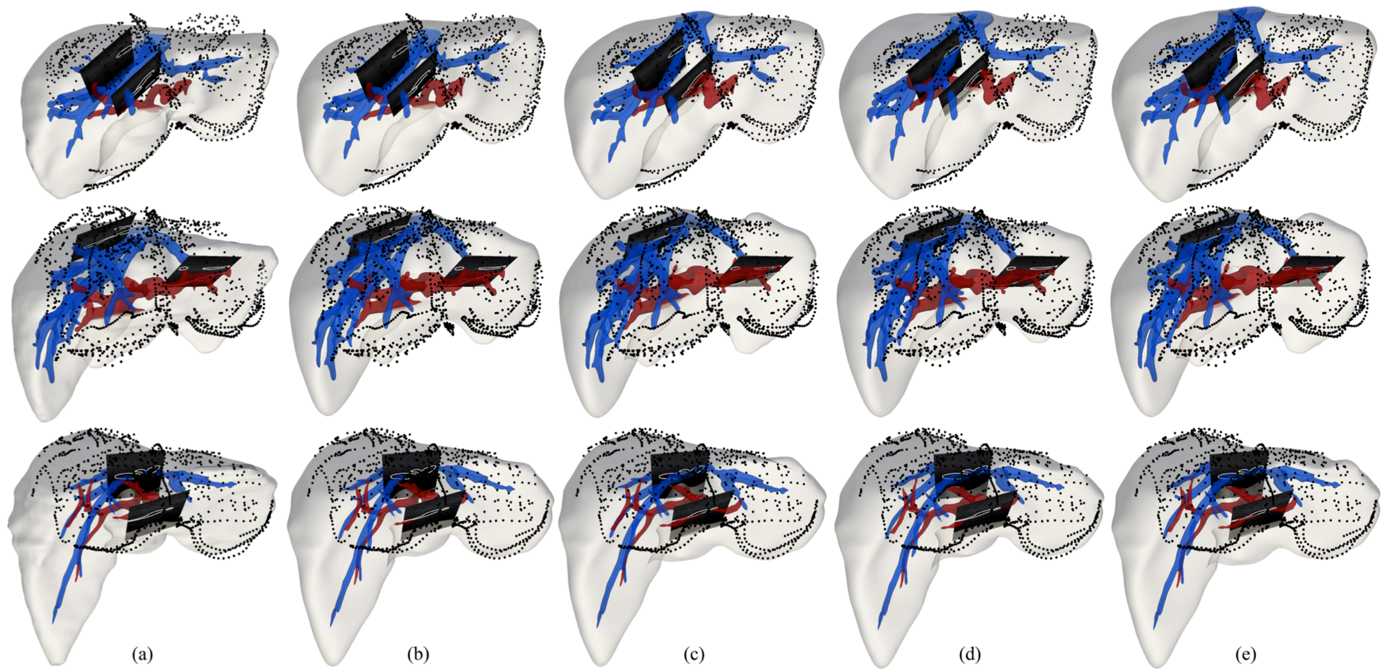

Fig. 8. Registered liver models (white surface) to surface data (black points) and features from tracked iUS (white points) for three clinical cases of image-guided open liver surgery (A – top; B – middle; C – bottom). Hepatic and portal vein vessel branches are shown in blue and red, respectively. (a) Rigid registration to surface data. (b) Deformable registration to surface data. (c) Deformable registration to surface data and the portal vein. (d) Deformable registration to surface data and the hepatic vein. (e) Deformable registration to surface data and the portal and hepatic veins.

one another (two sample K–S test, $\alpha = 0.001$). It is interesting to note that TRE is lower for registrations to all 16 iUS planes and sparse surface data than for registrations that could access the full anterior and posterior surfaces with CBCT, suggesting that reconstructive capacity could be superior with scattered iUS coverage of internal structures and sparse surface data than with thorough coverage of the surface but no subsurface information.

D. Clinical Experiments

Clinical data with tracked iUS were acquired from three patients undergoing open liver resection with informed consent and approval of the institutional review board at Memorial Sloan Kettering Cancer Center. Data were collected as described in section II-A and analyzed retrospectively. Two tracked ultrasound planes from each patient were selected on the criteria that each plane included vessel features of only the portal vein or only the hepatic vein, and each plane was separated by at least 3 cm. The distances between ultrasound plane features were 3.4 cm in the first patient (Case A), 8.3 cm in the second patient (Case B), and 6.5 cm in the third patient (Case C).

In the analysis, ultrasound plane features were used alternately as validation targets or sources of registration data. Rigid registration, deformable registration based on surface data, and deformable registration based on surface data augmented by the vessel contour, centerline, and posterior features visible in the tracked iUS plane were compared. To measure registration error, the average feature error is defined as the average distance between the iUS vessel contour points and the closest points on the registered vessel model. This metric is chosen because corresponding target points cannot be determined between the iUS image plane and the preoperative CT volume with high certainty. The feature errors from the three clinical cases are shown graphically in Fig. 8 and tabulated in Table III. Overall, the average feature error of the six validation targets improved 67% over rigid registration and 56% over deformable surface registration when incorporating data from the independent iUS plane. These substantial improvements were obtained under real sources of clinical noise, including tracking error, calibration error, physiological changes to the hepatic vasculature, and deformation induced by the tracked stylus and transducer.

TABLE III
FEATURE ERRORS (MM) FOR CLINICAL CASES

Registered Data	Case A Portal Feature Error	Case A Hepatic Feature Error	Case B Portal Feature Error	Case B Hepatic Feature Error	Case C Portal Feature Error	Case C Hepatic Feature Error
Rigid	10.8 ± 3.9 (17.0)	14.3 ± 1.8 (16.5)	4.1 ± 1.4 (7.2)	9.8 ± 1.5 (13.2)	5.4 ± 2.6 (10.0)	3.5 ± 2.0 (7.7)
Surface (S)	9.7 ± 3.6 (15.8)	12.0 ± 2.2 (15.1)	3.1 ± 1.7 (7.9)	3.2 ± 2.2 (9.9)	5.2 ± 3.5 (11.0)	3.1 ± 2.1 (8.0)
S + Portal	*1.3 ± 0.9 (3.6)*	2.9 ± 1.9 (6.2)	*0.9 ± 0.6 (2.5)*	1.3 ± 1.0 (4.2)	*1.0 ± 0.8 (2.9)*	3.0 ± 2.3 (9.1)
S + Hepatic	3.5 ± 3.1 (10.6)	*0.8 ± 0.5 (1.9)*	1.6 ± 1.3 (5.2)	*1.1 ± 0.7 (3.1)*	3.6 ± 2.5 (8.1)	*0.8 ± 0.7 (0.3)*
S + Portal + Hepatic	*1.3 ± 0.9 (3.4)*	*0.7 ± 0.4 (1.5)*	*0.8 ± 0.5 (2.2)*	*1.2 ± 0.8 (3.8)*	*1.1 ± 0.7 (2.8)*	*0.9 ± 0.7 (0.4)*

A summary of feature registration errors for portal and hepatic contours from tracked iUS planes in clinical cases A (left), B (center), and C (right). Rows show the feature errors for rigid registration, deformable registration based on surface data (S), and deformable registrations with additional subsurface data. Maximum values of the closest point feature distance are shown in parentheses. Values in italics mark residual error of the features used for registration.

While noise sources were not specifically addressed in simulation studies, these preliminary clinical results suggest that the reconstruction method can perform remarkably well in realistic situations.

IV. Discussion

The results show that in challenging configurations of organ deformation and data coverage, large improvements can be made to registration accuracy by incorporating sparse features from tracked intraoperative ultrasound. Although feature errors reported for the clinical data are lower than the best TRE values from simulated data, it must be emphasized that these error metrics are not directly comparable. Because single corresponding target points cannot be exactly determined from the iUS planes, the clinical metric requires the error of iUS feature points to be projected onto the registered vessel model. This projected feature error has the effect of underestimating the true TRE. Additionally, feature errors from the clinical experiments are sampled at a single location in the liver whereas the simulated TRE metric averages the error over every vertex in the meshed domain. The simulated TRE values presented in Table II account for whole organ registration error, representing a more difficult test configuration that rewards accurate predictions of deformation beyond the immediate region of data collection.

In the context of boundary value reconstruction, rich data can be derived from iUS to produce informative subsurface feature constraints that capture information about organ deformation normally inaccessible by surface digitization tools. However, in the context of clinical workflow, tracked iUS can be difficult to implement and interpret, necessitating a judicious balance between maximizing interventional benefit and minimizing intraoperative disturbance. This work shows that a variety of anatomical features visible in a small number of tracked iUS planes of the liver can significantly improve the accuracy of registration throughout the entire organ.

Regarding benchmarks for intraoperative data collection and computation time, surface points and tracked iUS planes can be collected and processed within 60 seconds. While rigid registration can be performed at frame rate, the reconstructive component of the clinical registrations completed in 37.6 ± 5.4 seconds. These registrations were performed on a single thread of a 4.0 GHz Intel Core i7 CPU. Although the total intraoperative computational burden is already low, parallelizing the model-data error and gradient computations shown in Table 1 could further reduce the computation time. Despite manual iUS feature designation limiting continuous real-time potential, we have shown that it is possible to perform intermittent high quality registrations by estimating the deformation state vector $\boldsymbol{\beta}$. In the future, further accelerations can be made as computational efficiency continues to improve and automatic iUS vessel segmentation and surface acquisition methods become more advanced.

Another factor that affects the computational complexity is the resolution with which spatial variations in the boundary load can be reconstructed. A sufficiently large number of control points k can improve the reconstructive capacity and potentially lead to more accurate registrations. However, excessive k introduces additional degrees of freedom to the reconstructive basis that can lead to prohibitive computation cost and degrade the conditioning of the inverse problem to the point where the solution is inadequately determined by intraoperative data constraints. This relationship between TRE, the model resolution k, and the amount of data coverage is shown in Fig. 9. Though the best value of k that minimizes TRE depends on the amount of intraoperative data, the shallow minima suggest low sensitivity. The value $k = 45$ offers a good tradeoff between these considerations for the typical size of a human liver, intraoperative time constraints, and the amount of data that can be collected to resolve the reconstruction to a level of accuracy that meets clinical need.

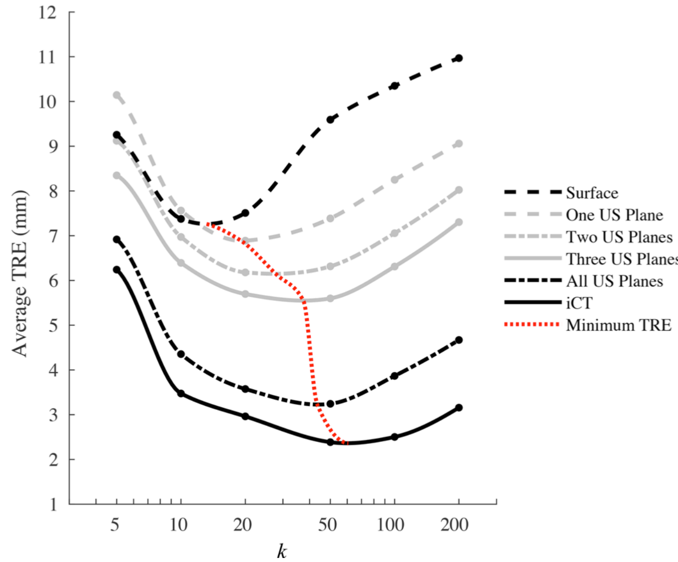

Fig. 9. Plot of average TRE values for registrations from simulated data 1–L across the number of control points k and the extent of intraoperative data available for registration. Lines were interpolated from six evaluation points with a cubic spline. The optimal value of k that minimizes TRE based on intraoperative data coverage, marked by the dotted red line, depends on a tradeoff between reconstructive model resolution and the ability to sufficiently constrain the degrees of freedom in the model.

With regard to limitations, while the simulated data show that adding the first, second, and third iUS planes to the deformable surface registration incrementally improves TRE across the mesh, the average TRE values from Table II include all potential combinations of simulated iUS plane positions. The relative value of each plane was not considered in relation to the redundancy of nearby data and the profile of intraoperative deformation, causing the average TRE values to be higher than the best achievable. In registrations to the ground truth deformation 1–L, the smallest average TRE with a single iUS plane was 4.9 ± 3.0 mm and the smallest average TRE with three iUS planes was 3.9 ± 2.5 mm. With 5 mm representing the clinical goal for accuracy at half the recommended oncological margin, the ability to overcome this threshold over the entire liver volume is possible with very sparse iUS coverage. While outside the scope of this paper, it may be possible to strategically plan favorable configurations of tracked iUS data collection in targeted regions to reliably decrease TRE with a predictive registration assessment

This article has been accepted for publication in a future issue of this journal, but has not been fully edited. Content may change prior to final publication. Citation information: DOI 10.1109/TMI.2020.2967322, IEEE Transactions on Medical Imaging

framework for data sufficiency. Even so, the results from Table II show that registering 16 distributed iUS planes can easily exceed the benchmark of 5 mm average TRE. As a general guide for positioning iUS planes in sparser coverage, it can be inferred from Fig. 6 that even spacing can be an effective strategy for improving registration accuracy so as to reduce the overall target-data distance shown in Fig. 5d. In the clinical experiments, while validation is less comprehensive, similarly compelling local improvements to subsurface accuracy are shown when iUS features can be used to augment surface data during registration. While these preliminary results are promising, more extensive clinical validation is eventually needed to demonstrate the ability of the algorithm to accurately reconstruct deformation responses of real tissue.

V. Conclusion

In this paper, a linearized iterative boundary reconstruction method for compensating intraoperative deformation of the liver using sparse surface and subsurface data is proposed. Information from tracked iUS was incorporated into the registration methodology and its impact was characterized with an expansive simulated dataset. Feasibility was also demonstrated in three clinical cases. Findings show that incorporating information from sparse intraoperative ultrasound can make significant improvements to registration accuracy for hepatic image guidance, and that strategic combinations of sparse data might have the potential to outperform seemingly more dense configurations of data.

References

[1] J. S. Heiselman, L. W. Clements, J. A. Collins, J. A. Weis, A. L. Simpson, S. K. Geevarghese, *et al.*, "Characterization and correction of soft tissue deformation in laparoscopic image-guided liver surgery," *J. Med. Imaging*, vol. 5, no. 2, pp. 1–13, 2018.

[2] S. Suwelack, S. Röhl, S. Bodenstedt, D. Reichard, R. Dillmann, T. dos Santos, *et al.*, "Physics-based shape matching for intra-operative image guidance," *Med. Phys.*, vol. 41, pp. 1–12, 2014.

[3] R. Plantefève, I. Peterlik, N. Haouchine, and S. Cotin, "Patient-Specific Biomechanical Modeling for Guidance During Minimally-Invasive Hepatic Surgery," *Ann. Biomed. Eng.*, vol. 44, no. 1, pp. 139–153, 2016.

[4] R. Modrzejewski, T. Collins, B. Seeliger, A. Bartoli, A. Hostettler, and J. Marescaux, "An in vivo porcine dataset and evaluation methodology to measure soft-body laparoscopic liver registration accuracy with an extended algorithm that handles collisions," *Int. J. Comput. Assist. Radiol. Surg.*, vol. 14, no. 7, pp. 1237–1245, 2019.

[5] D. Reichard, D. Häntsch, S. Bodenstedt, S. Suwelack, M. Wagner, H. Kenngott, *et al.*, "Projective biomechanical depth matching for soft tissue registration in laparoscopic surgery," *Int. J. Comput. Assist. Radiol. Surg.*, vol. 12, no. 7, pp. 1101–1110, 2017.

[6] E. Özgür, B. Koo, B. Le Roy, E. Buc, and A. Bartoli, "Preoperative liver registration for augmented monocular laparoscopy using backward–forward biomechanical simulation," *Int. J. Comput. Assist. Radiol. Surg.*, vol. 13, no. 10, pp. 1629–1640, 2018.

[7] L. W. Clements, J. A. Collins, J. A. Weis, A. L. Simpson, T. P. Kingham, W. R. Jarnagin, *et al.*, "Deformation correction for image-guided liver surgery: An intraoperative assessment of fidelity," *Surgery*, vol. 162, no. 3, pp. 537–547, 2017.

[8] D. C. Rucker, Y. Wu, L. W. Clements, J. Ondrake, T. Pheiffer, A. L. Simpson, *et al.*, "A Mechanics-Based Nonrigid Registration Method for Liver Surgery using Sparse Intraoperative Data.," *IEEE Trans. Med. Imaging*, vol. 33, no. 1, pp. 147–158, 2014.

[9] J. A. Collins, J. A. Weis, J. S. Heiselman, L. W. Clements, A. L. Simpson, W. R. Jarnagin, *et al.*, "Improving Registration Robustness for Image-Guided Liver Surgery in a Novel Human-to-Phantom Data Framework," *IEEE Trans. Med. Imaging*, vol. 36, no. 7, pp. 1502–1510, 2017.

[10] H. G. Kenngott, M. Wagner, M. Gondan, and F. Nickel, "Real-time image guidance in laparoscopic liver surgery: first clinical experience with a guidance system based on intraoperative CT imaging," *Surg Endosc*, vol. 28, pp. 933–940, 2013.

[11] I. Peterlík, H. Courtecuisse, R. Rohling, P. Abolmaesumi, C. Nguan, S. Cotin, *et al.*, "Fast elastic registration of soft tissues under large deformations," *Med. Image Anal.*, vol. 45, pp. 24–40, 2018.

[12] L. Viganò, A. Ferrero, M. Amisano, N. Russolillo, and L. Capussotti, "Comparison of laparoscopic and open intraoperative ultrasonography for staging liver tumours," *Br. J. Surg.*, vol. 100, pp. 535–542, 2013.

[13] T. P. Kingham, L. M. Pak, A. L. Simpson, U. Leung, A. Doussot, M. I. D'Angelica, *et al.*, "3D image guidance assisted identification of colorectal cancer liver metastases not seen on intraoperative ultrasound: results from a prospective trial," *HPB*, vol. 20, no. 3, pp. 260–267, 2018.

[14] J. M. Blackall, G. P. Penney, A. P. King, A. N. Adam, and D. J. Hawkes, "Tracking alignment of sparse ultrasound with preoperative images of the liver and an interventional plan using models of respiratory motion and deformation," *IEEE Trans. Med. Imaging*, vol. 24, no. 11, pp. 1405–1416, 2005.

[15] M. Nakamoto, H. Hirayama, Y. Sato, K. Konishi, Y. Kakeji, M. Hashizume, *et al.*, "Recovery of respiratory motion and deformation of the liver using laparoscopic freehand 3D ultrasound system," *Med. Image Anal.*, vol. 11, no. 5, pp. 429–442, 2007.

[16] W. Wein, S. Brunke, A. Khamene, M. R. Callstrom, and N. Navab, "Automatic CT-ultrasound registration for diagnostic imaging and image guided intervention," *Med. Image Anal.*, vol. 12, pp. 577–585, 2008.

[17] D. Lee, W. H. Nam, J. Y. Lee, and J. B. Ra, "Non-rigid registration between 3D ultrasound and CT images of the liver based on intensity and gradient information," *Phys. Med. Biol.*, vol. 56, pp. 117–137, 2011.

[18] M. Yang, H. Ding, J. Kang, L. Cong, L. Zhu, and G. Wang, "Local structure orientation descriptor based on intra-image similarity for multimodal registration of liver ultrasound and MR images," *Comput. Biol. Med.*, vol. 76, pp. 69–79, 2016.

[19] T. Lange, N. Papenberg, S. Heldmann, J. Modersitzki, B. Fischer, H. Lamecker, *et al.*, "3D ultrasound-CT registration of the liver using combined landmark-intensity information," *Int. J. Comput. Assist. Radiol. Surg.*, vol. 4, no. 1, pp. 79–88, 2009.

[20] N. Archip, S. Tatli, P. R. Morrison, F. Jolesz, S. K. Warfield, and S. G. Silverman, "Non-rigid registration of pre-procedural MR images with intra-procedural unenhanced CT images for improved targeting of tumors during liver radiofrequency ablations," *Med. Image Comput. Comput. Interv.*, vol. 10, no. 2, pp. 969–977, 2007.

[21] Y. Song, J. Totz, S. Thompson, S. Johnsen, D. Barratt, C. Schneider, *et al.*, "Locally rigid, vessel-based registration for laparoscopic liver surgery," *Int. J. Comput. Assist. Radiol. Surg.*, vol. 10, pp. 1951–1961, 2015.

[22] F. Nazem, A. Ahmadian, N. D. Seraj, and M. Giti, "Two-stage point-based registration method between ultrasound and CT imaging of the liver based on ICP and unscented Kalman filter: A phantom study," *Int. J. Comput. Assist. Radiol. Surg.*, vol. 9, no. 1, pp. 39–48, 2014.

[23] J. Ramalhinho, M. R. Robu, S. Thompson, K. Gurusamy, B. Davidson, D. Hawkes, *et al.*, "A pre-operative planning framework for global registration of laparoscopic ultrasound to CT," *Int. J. Comput. Assist. Radiol. Surg.*, vol. 13, no. 8, pp. 1177–1186, 2018.

[24] L. W. Clements, J. A. Collins, A. L. Simpson, L. B. Adams, W. R. Jarnagin, and M. I. Miga, "Evaluation of model-based deformation correction in image-guided liver surgery via tracked intraoperative ultrasound," *J. Med. Imaging*, vol. 3, no. 1, pp. 1–10, 2016.

[25] D. M. Cash, M. I. Miga, T. K. Sinha, R. L. Galloway, and W. C. Chapman, "Compensating for intraoperative soft-tissue deformations using incomplete surface data and finite elements," *IEEE Trans. Med. Imaging*, vol. 24, no. 11, pp. 1479–1491, 2005.

[26] P. Dumpuri, L. W. Clements, B. M. Dawant, and M. I. Miga, "Model-updated image guided liver surgery: preliminary results using surface characterization," *Prog. Biophys. Mol. Biol.*, vol. 103, pp. 197–207, 2010.

[27] A. L. Simpson, D. A. Geller, A. W. Hemming, W. R. Jarnagin, L. W. Clements, M. I. D'Angelica, *et al.*, "Liver planning software accurately predicts postoperative liver volume and measures early regeneration," *J. Am. Coll. Surg.*, vol. 219, no. 2, pp. 199–207, 2014.

[28] L. Antiga, M. Piccinelli, L. Botti, B. Ene-Iordache, A. Remuzzi, and D. A. Steinman, "An image-based modeling framework for patient-specific computational hemodynamics," *Med. Biol. Eng. Comput.*, vol. 46, no. 11, pp. 1097–1112, 2008.

[29] J. M. Sullivan, G. Charron, and K. D. Paulsen, "A three-dimensional mesh generator for arbitrary multiple material domains," *Finite Elem. Anal. Des.*, vol. 25, pp. 219–241, 1997.
[30] D. M. Cash, M. I. Miga, S. C. Glasgow, B. M. Dawant, L. W. Clements, Z. Cao, *et al.*, "Concepts and preliminary data toward the realization of image-guided liver surgery," *J. Gastrointest. Surg.*, vol. 11, no. 7, pp. 844–859, 2007.
[31] T. K. Chen, A. D. Thurston, R. E. Ellis, and P. Abolmaesumi, "A real-time freehand ultrasound calibration system with automatic accuracy feedback and control," *Ultrasound Med. Biol.*, vol. 35, pp. 79–93, 2009.
[32] T. P. Kingham, M. A. Scherer, B. W. Neese, L. W. Clements, J. D. Stefansic, and W. R. Jarnagin, "Image-guided liver surgery: Intraoperative projection of computed tomography images utilizing tracked ultrasound," *HPB*, vol. 14, no. 9, pp. 594–603, 2012.
[33] J. E. Bresenham, "Algorithm for computer control of a digital plotter," *IBM Syst. J.*, vol. 4, no. 1, pp. 25–30, 1965.
[34] L. W. Clements, W. C. Chapman, B. M. Dawant, R. L. Galloway, and M. I. Miga, "Robust surface registration using salient anatomical features for image-guided liver surgery: algorithm and validation.," *Med. Phys.*, vol. 35, no. 6, pp. 2528–2540, 2008.
[35] B. Vallet and B. Lévy, "Spectral Geometry Processing with Manifold Harmonics," *Eurographics*, vol. 27, no. 2, 2008.
[36] T. Möller, "A fast triangle-triangle intersection test," *J. Graph. Tools*, vol. 2, no. 2, pp. 1–5, 1997.